

# Melting Layer Attenuation as Observed by Polarimetric Radar-Radiometer Synergistic Approach

Pablo Saavedra G.<sup>1</sup>, Alessandro Battaglia<sup>2</sup>, Alexander Ryzhkov<sup>3</sup>, and Clemens Simmer<sup>4</sup>

<sup>1</sup>*Meteorological Institute, University of Bonn, Auf dem Huelgel 20, 53121 Bonn, Germany*

<sup>2</sup>*Department of Physics and Astronomy, University of Leicester, UK*

<sup>3</sup>*University of Oklahoma and NOAA/OAR/National Severe Storm Laboratory, Norman, OK, USA*

<sup>4</sup>*Meteorological Institute, University of Bonn, Auf dem Huelgel 20, 53121 Bonn, Germany*

(Dated: 19 September 2014)



Pablo Saavedra G.

## 1. Introduction

Melting layer is the main mechanism responsible for the conversion of solid precipitating into liquid during stratiform rain. Melting layer is characterized by a mixed phase nature making it difficult to estimate its micro-physic properties, hence its related attenuation. Therefore modellers need to assume a certain composition of water/ice electromagnetic properties in order to assess radar related parameters (Matrosov, 2008). The present contribution is a new approach to estimate melting layer attenuation from combined passive-active synergistic measurements.

The development of methods for Quantitative Precipitation Estimation (QPE) by dual-polarimetry weather radars provides a robust set of tools to estimate attenuation for the rain layer. On the other hand, the multi-frequency dual-polarized radiometer ADMIRARI has shown its capabilities to simultaneously estimate water vapour, and precipitating clouds parameters, e.g. the slant path integrated water vapour, rain and cloud water content (Battaglia et al., 2009, 2010; Saavedra et al., 2012a). The microwave radiometer (MWR) brightness temperatures can as well be used to provide an estimation of the path integrated attenuation (PIA) from the slant column, thereafter two independent estimations are obtained, i.e. from the radar and from the radiometer, and the melting layer attenuation might be estimated by combining the passive and active PIA retrievals.

Previous work by Saavedra et al. (2012b, LPVEx campaign) has shown that when the rain attenuation is not properly estimated it might lead to non-physical results, this specially true for light rain where polarimetry methods are insufficient.

The attenuation due to the melting layer might be estimated under the condition that any difference between the estimated PIA by the passive and active sensors are due to the melting layer. Considering the multi-frequency feature of ADMIRARI, this estimation might also be extended to X, K and Ka-band.

## 2. Measuring Precipitation by Active and Passive Sensors

For the present study two instruments are being used to measure precipitation, namely a X-band dual-polarimetric weather radar and the radiometer ADMIRARI.

### 2.1. X-band dual-pol weather radar

The Jülich Research Center possesses an operational X-band polarimetric weather radar (JuXPol), which is part of the twin X-band radar system located at Bonn (BoXPol) and Sophienhöhe nearby Jülich in Germany. The main features of the radar are:

*Table 1: Radar's main characteristics.*

Frequency	9.3 GHz
Wavelength	3.2 cm
Band-width	200 MHz
Beam-width	1.03° FWHM
Maximum range	50 km
Range resolution	150 m
Pulse power	200 kW
Mean sending power	150 W
Angular resolution	0.2°

The radar coordinates are 50° 54' 32.5'' latitude, and 6° 24' 43.2'' longitude. The standard observation strategy is comprised of a volume scan with 10 elevation angles every 5 minutes to produce a composite product together with its twin radar in Bonn; in between the radar performs an elevation scan (RHI from 0 to 90°) towards the Jülich Research Facility i.e. 234° azimuth.

The radar products includes the following moments: attenuated reflectivity in horizontal and vertical polarization, differential reflectivity, cross-correlation coefficient and differential phase factor and specific differential phase.

## 2.2. Radiometer ADMIRARI

The University of Bonn's **AD**vanced **MI**crowave **RA**diometer for **R**ain **I**dentification (ADMIRARI) is a triple-frequency (10.7, 21.0 and 36.5 GHz) dual-polarized (H & V) scanning passive microwave radiometer (MWR) Battaglia et al. (2009). The polarization capabilities give the ability to distinguish the signature from rain and pure cloud. Therefore the retrieval of slant integrated water vapour, and liquid water path (LWP) in its cloud and rain component is the state-of-the-art products Battaglia et al. (2010); Saavedra et al. (2012a).



Figure 1: The picture shows the radiometer ADMIRARI. With its rain radar (right) and a cloud lidar (left) attached to the pedestal.

The ADMIRARI MWR additionally comprises of two co-located ancillary instruments, i.e. a 24.1 GHz micro rain radar and a 905 nm cloud Lidar.

Table 2: Radiometer's main characteristics.

Band	X	K	Ka
Frequencies [GHz]	10.7	21.0	36.5
Wavelength [cm]	2.80	1.43	0.82
Band-width [MHz]	500	500	400
Beam-width FWHM	$\sim 6^\circ$ all channels		
Integration time	2 sec. all channels		

Typical ADMIRARI data set comprise of Brightness Temperature (V & H), Polarization Difference (V - H), reflectivity factor at 24.1 GHz and backscattering factor at 902 nm (figure 2).

## 2.3. Measurements strategy

ADMIRARI is installed since end of April 2013 at the JFZ facility and set-up to measure on elevation mode ( $30^\circ$  elevation and RHI scans) and same azimuth as the JuXPOL radar's RHI scans. The relative distance between both instruments is 3.8 km with the radiometer located south-west from JuXPOL. The radar's RHI scans swept the radiometer's observation scene with  $0.2^\circ$  elevation steps, ensuring a good spatial resolution.

For the present study, observations from June 20th 2013 are utilized. Precipitation was characterized by 4 main rain events along the day, with periods lasting from couple of hours to 4 hours. Figures 2 and 3 give an overview to the data collected by ADMIRARI and JuxPol respectively. During the morning and midday, precipitation was observed mostly as stratiform rain with freezing level around 3 km for the most of the time. From 20:00UTC the precipitation regime has changed to convective storm (c.a. 21:00UTC) embedded in a stratiform rain (see right-bottom panel in figure 3).

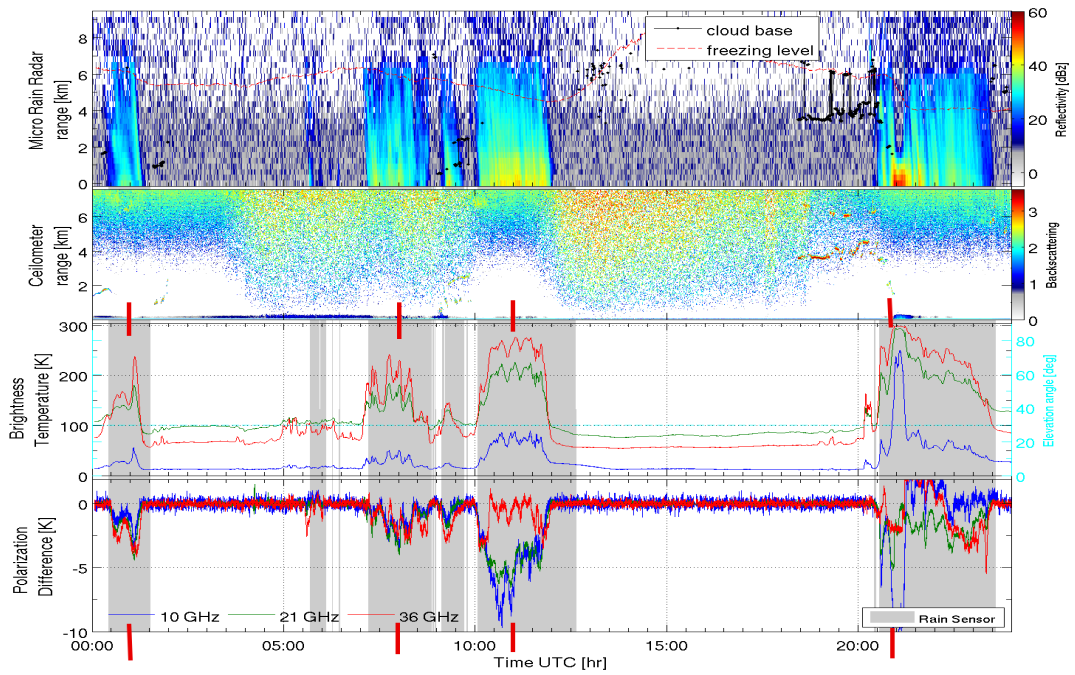


Figure 2: ADMIRARI time series of Brightness Temperatures and Polarization Difference at 10.7 (blue), 21.0 (green) and 36.5 (red) GHz. Case study from June 20th, 2013. Gray area represent rain periods.

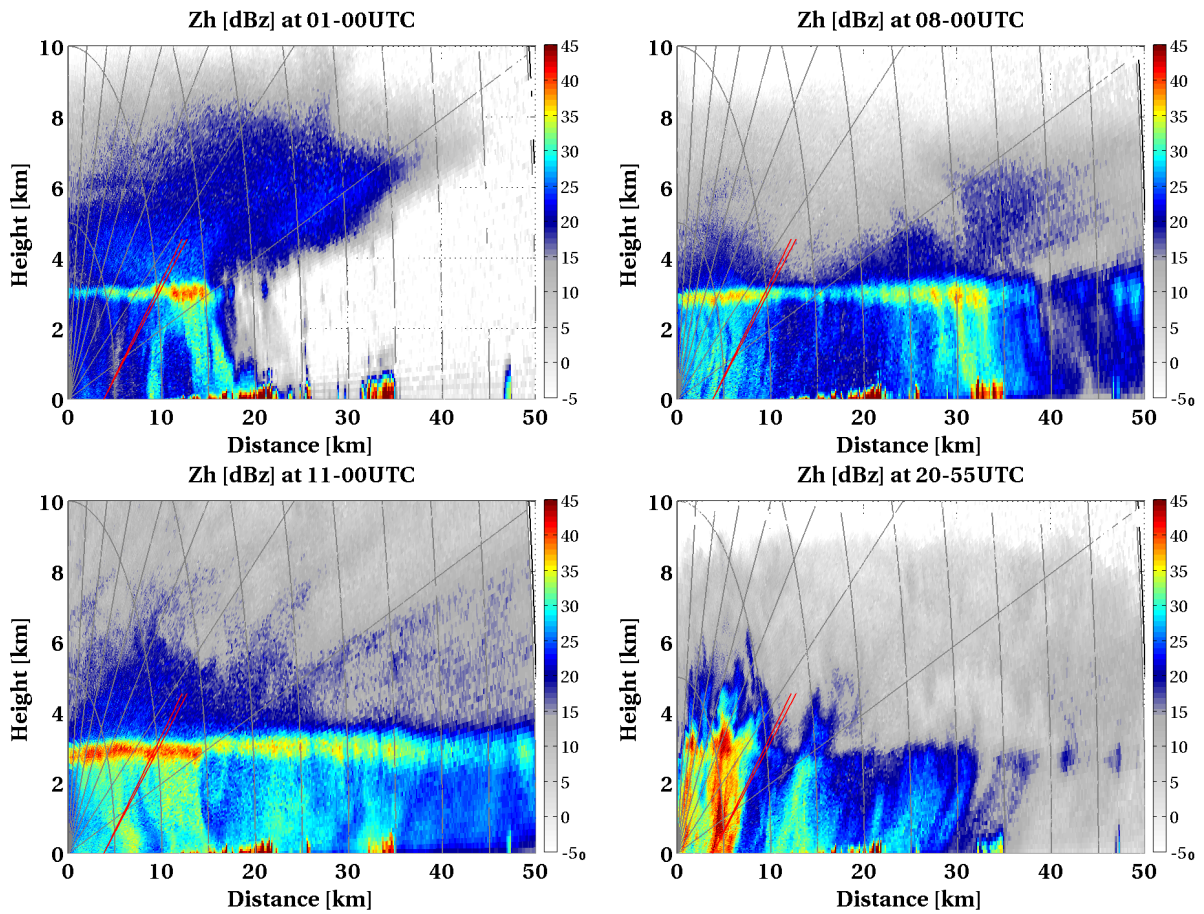


Figure 3: JuXPOL radar reflectivity RHI scans at same ADMIRARI's azimuth. Red cone at 3.8 km represents the instantaneous radiometer FOV.

### 3. Retrieval for attenuation from two independent methods

#### 3.1. Specific Attenuation from dual-pol Radar

In order to estimate the specific attenuation from X-band polarimetric radar, the ZPHI method is exploited (Bringi and Chandrasekar, 2001; Testud et al., 2000).

The ZPHI method is commonly used in Quantitative Precipitation Estimation (QPE) applied to radar PPI scans. The technique couples the profiles of attenuated reflectivity e.g.  $Z_h(r)$  and the differential phase shift  $\Phi_{dp}(r)$ . It assumes that attenuation  $A(r)$  is related to reflectivity as  $A(r) = a(r) [Z(r)]^{b(r)}$ , where  $Z(r)$  is the intrinsic reflectivity factor, and the coefficients  $a$  and  $b$  are frequency and temperature dependent. Following the power law equation which relates attenuation with reflectivity and the relationship between attenuation with the specific differential phase  $K_{dp}$

$$A(r) = \alpha(r) K_{dp} \quad , \text{ where } K_{dp} = \frac{\Delta\Phi}{2 \Delta r}$$

the following equation can be derived (for the detailed derivation, see Bringi and Chandrasekar (2001); Testud et al. (2000)):

$$A(r) = \frac{a(r) [Z_h(r)]^{b(r)} [\exp(0.23 b(r) PIA) - 1]}{I_a(r_0, r_{top}) + [\exp(0.23 b(r) PIA) - 1] I_a(r, r_{top})}, \quad (3.1)$$

in  $[\text{dB km}^{-1}]$  units and with

$$I_a(r, r_{top}) = 0.46 \int_r^{r_{top}} b(s) a(s) [Z_h(s)]^{b(s)} ds \quad (3.2)$$

Here  $Z_h$  is the measured radar reflectivity and the integration must be performed till the top of the rain layer  $t_{top}$ . The Path Integrated Attenuation (PIA) in equation 3.1 is given as a function of the gradient on differential phase shift  $\Delta\Phi$  as follow (Bringi and Chandrasekar (2001); Ryzhkov et al. (2014); Testud et al. (2000)):

$$PIA = \alpha(r) \Delta\Phi \quad (3.3)$$

with

$$\Delta\Phi = \Phi_{dp}(r_{top}) - \Phi_{dp}(r_0) \quad (3.4)$$

Equation 3.1 is presented in its most general form. A common practice, however, is to assume the coefficients  $a$  and  $b$  to be constant along the path. This leads to the following simplification in equation 3.1: the coefficient  $a$  can be cancelled out from numerator and denominator, and coefficient  $b$  can be set outside the integration as an invariant (Ryzhkov et al., 2014). These two assumptions are acceptable since the ZPHI method is typically applied to PPI scans at low elevation angles e.g.  $0.5$  to  $1.5^\circ$ .

Once  $A(r)$  is computed for every range gate, PIA can be calculated for any arbitrary path and path-length within the radar RHI 2-D field, given by

$$PIA = \int_{s_0}^{s_{top}} [A(r)] dr, \quad [\text{dB}] \quad (3.5)$$

#### 3.2. Attenuation from Radiometry

The most common method to estimate the attenuation from microwave radiometric measurements comprises of solving the analytical expression for the radiative transfer equation in the Rayleigh-Jeans approximation, leading to an expression for the optical thickness (atmospheric opacity) as a function of the brightness temperature, given by (e.g. Gaussiat et al., 2007; Mätzler and Morland, 2009)

$$\tau(\nu) = -\mu \ln \left( \frac{TB_{mr}(\nu) - TB_\nu}{TB_{mr}(\nu) - TB_{cmb}} \right) \quad (3.6)$$

where  $\tau$  is the optical thickness,  $\mu$  is the cosine of the zenithal angle of radiometric observations,  $\nu$  represents the frequency,  $TB_{mr}$  is the atmospheric mean radiating temperature,  $TB_{cmb} \sim 2.73 \text{ K}$  is the cosmic microwave background radiation, and  $TB_\nu$  is the measured brightness temperature.

Nevertheless the equation 3.6, derived from a 1-D plane parallel atmospheric model, is not appropriated for precipitation events since rain drops produce significant scattering effects with uneven magnitudes at every frequency. Thus a different approach is needed in order to take into account emission, absorption and scattering by rain drops.

In that sense, the ADMIRARI's Bayesian retrieval scheme developed for retrievals of rain and cloud liquid water path (Battaglia et al., 2009; Saavedra et al., 2012a) has been extended to retrieve also the optical thickness of cloud, rain and water vapour.

Bayesian theory is a general approach for solving inverse problems, i.e. the estimation of the true state of the atmosphere from indirect observations given *a priori* information on the expected atmospheric state. In our application the measurement vector  $\vec{y}_O$  contains spectral brightness temperatures and related polarization differences, which are assumed to be affected by random errors described by an error covariance matrix  $\mathcal{O}$ . The state vector  $\vec{x}$  contains the profiles of all atmospheric parameters (e.g. water vapour, temperature, cloud liquid water, rain water, DSD, ...), which affect the measurement vector. Bayesian theory states that the inverse problem can be related to the forward problem through a set of measurements and prior knowledge about the probability of the state vector by (see e.g. (Marzano et al., 1999; McFarlane et al., 2002))

$$P_{post}(\vec{x}|\vec{y}_O) = \frac{P_f(\vec{y}_O|\vec{x}) P_{pr}(\vec{x})}{\int P_f(\vec{y}_O|\vec{x}) P_{pr}(\vec{x}) d\vec{x}}, \quad (3.7)$$

with  $P_{post}(\vec{x}|\vec{y}_O)$  the conditional probability of the state vector  $\vec{x}$  given the observations  $\vec{y}_O$ ,  $P_{pr}(\vec{x})$  the *a priori* probability of the state vector  $\vec{x}$  before the measurement is made, and  $P_f(\vec{y}_O|\vec{x})$  the conditional (or forward) probability of the measurement  $\vec{y}_O$  given the state vector  $\vec{x}$ .

The probability  $P_f(\vec{y}_O|\vec{x})$  can be modelled from the distribution of observations close to the simulated synthetic observation  $\vec{y}_S(\vec{x})$ , with the width of the distribution governed by the measurement and the model errors. If these errors can be assumed to be Gaussian and uncorrelated, then the probability of observational deviations may be expressed as

$$P_f(\vec{y}_O|\vec{x} = \vec{x}_{true}) \propto P([\vec{y}_O - \vec{y}_S(\vec{x})]),$$

with

$$P([\vec{y}_O - \vec{y}_S(\vec{x})]) \propto \exp\left\{-\frac{1}{2}([\vec{y}_O - \vec{y}_S(\vec{x})]^T \mathcal{C}^{-1} [\vec{y}_O - \vec{y}_S(\vec{x})])\right\} \quad (3.8)$$

where  $\mathcal{C}$  is the error covariance matrix of the simulation error plus the instrument noise i.e.  $\mathcal{O} + \mathcal{S}$ . For simplification we denote the residuals as

$$[\vec{y}_O - \vec{y}_S(\vec{x})]^T \mathcal{C}^{-1} [\vec{y}_O - \vec{y}_S(\vec{x})] = \delta^2. \quad (3.9)$$

When substituting Eqs. (3.8) and (3.9) into (3.7) the posterior PDF may be rewritten as

$$P_{post}(\vec{x}|\vec{y}_O) = \frac{\exp(-\frac{1}{2} \delta^2) P_{pr}(\vec{x})}{\int \exp(-\frac{1}{2} \delta^2) P_{pr}(\vec{x}) d\vec{x}}. \quad (3.10)$$

To obtain the expected (in the adopted formulation the mean) state vector, the state vector  $\mathbf{x}$  is integrated over its phase space weighted with the posterior PDF, i.e.

$$\langle \vec{x} \rangle = \int \vec{x} P_{post}(\vec{x}|\vec{y}_O) d\vec{x}. \quad (3.11)$$

The second moment of the posterior PDF gives an estimation of the retrieval uncertainty, namely the variance around the mean vector  $\langle \vec{x} \rangle$

$$\sigma_{\vec{x}}^2 = \int (\vec{x} - \langle \vec{x} \rangle)^2 P_{post}(\vec{x}|\vec{y}_O) d\vec{x} \quad (3.12)$$

By making the measurement we obtain a knowledge of the physical parameters and the *a priori* probability distribution function  $P_{pr}$  is narrowed toward a posterior PDF (eq. 3.10) of the variables that are retrieved.

In this context, the  $P_f(\vec{y}_O|\vec{x} = \vec{x}_{true})$  is obtained from the radiative transfer outputs i.e. forward model, while all atmospheric states are represented by vector  $\vec{x}$ . The variables we want to retrieve, for the present study, are represented by the vector  $\vec{y}$  as

$$\vec{y} = \begin{pmatrix} \tau_{\text{rain}}(\nu) \\ \tau_{\text{cloud}}(\nu) \\ \tau_{\text{wv}}(\nu) \end{pmatrix} \quad (3.13)$$

being  $\tau$  the frequency dependent optical thickness for rain, cloud and water vapour, and every  $\tau$  for both horizontal and vertical polarization.

In order to have a magnitude alike the path integrated attenuation (PIA) from equation 3.5, it is necessary to multiply by the factor  $10 \log_{10} e = 4.343$  to convert the values in equation 3.13 to decibels (dB) units.

#### 4. Synergy Radar-Radiometer

From the radar's RHI the equivalent radiometer's observation sector needed to be extracted. In order to do so, the radiometer's FOV is extracted from the radar according to the following considerations:



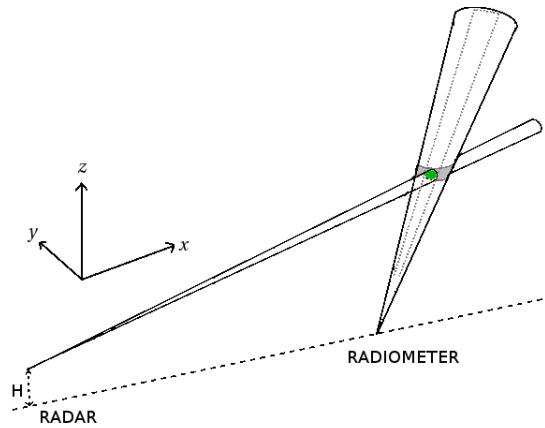


Figure 4: Schematics for the beam-width mismatching. The green area indicates the intersection of beams, while the surrounding gray area represents the required volume to be cover.

- Geometrical coordinates for both instruments, e.g. relative position and altitude,
- Instruments beam-width mismatching ( $\sim 6^\circ$  versus radar's  $1.3^\circ$ ),
- realistic radiometer's antenna pattern.

Figure 4 pictures some of the point listed above, with the distance radar-radiometer being of 3.8 km and a difference on altitude (H in figure 4) of 120 meters. Therefore at every radar beam's elevation angle, all the ranges which intersects the radiometer's FOV are isolated and their polar coordinates transformed from the radar reference to the radiometer's reference, for all elevation angles sweeping the radiometer FOV. The radar finer beam-width only intersects a small portion of the total required in order to properly fill the radiometer's FOV (green area versus gray area in the figure 4). To overcome this mismatching, the following geometrical consideration has been assumed, the factor obtained as the ratio of the volumes from radiometer and radar is used to expand the radar ranges laying inside the green frustum-cone to the volume inside the gray frustum-cone. This factor is used to multiply the values from the radar variables and extend them to the volume sensed by the radiometer, this under the assumption that the radar variables do not change considerable in that volume. For the lower radar elevation angles the factor is below 1 indicating that the radar frustum-cone is larger than the radiometer's one, at higher elevation angles the factor is greater than 1.

Another consideration is related to the radiometers antenna pattern. The method mentioned in the previous paragraph is only to fill the volume corresponding to the radiometers FOV, once the polar coordinates of radar bins which are inside the FOV are converted to radiometer's coordinates, it must be convoluted with the antenna pattern to obtain a realistic measurement. Therefore a Gaussian pattern with FWHM of  $3^\circ$  is assumed a good approximation of the real radiometer antenna.

If all those considerations are not being taking into account, synthetic biases might be created and thereafter jeopardize any attend to minimize uncertainties in the comparison or data fusion of both instruments. Those synthetic biases make difficult to interpret -for instance- the contribution from melting layer or other hydrometeor processes in the atmosphere when comparing rain LWP estimated from radar and radiometer independently (see for example (Saavedra et al., 2013, figure 8)).

## 5. Melting layer attenuation

### 5.1. Attenuation at X-band

The specific attenuation obtained from the radar by means of the ZPHI method (section 3.1) has been applied to observations from June 20th 2013. In figure 5 there is a set of results after applying the ZPHI method to the RHI scans in figure 3.

The radiometer's FOV has been extracted according to the considerations in section 4. Therefore any radar variable and retrieved parameter (e.g. specific attenuation, liquid water content, etc.) can be represented in slant profiles as they would have been observed by the radiometer. An integration over the slant path yields a radiometer-like measurement, which are later used to complement the stand-alone radiometer retrievals.

The present work is focused on the total attenuation produced by the rain layer. The residuals

$$\Delta \text{PIA} = \text{PIA}_{\text{MWR}} - \text{PIA}_{\text{RADAR}} \quad (5.1)$$

can be assumed as contributions introduced by the melting layer. Figure 6 depicts the X-band PIA from radiometer (gray-solid-line obtained from equation 3.13), overlapped to the radar's PIA (yellow-dots estimated with the ZPHI method).

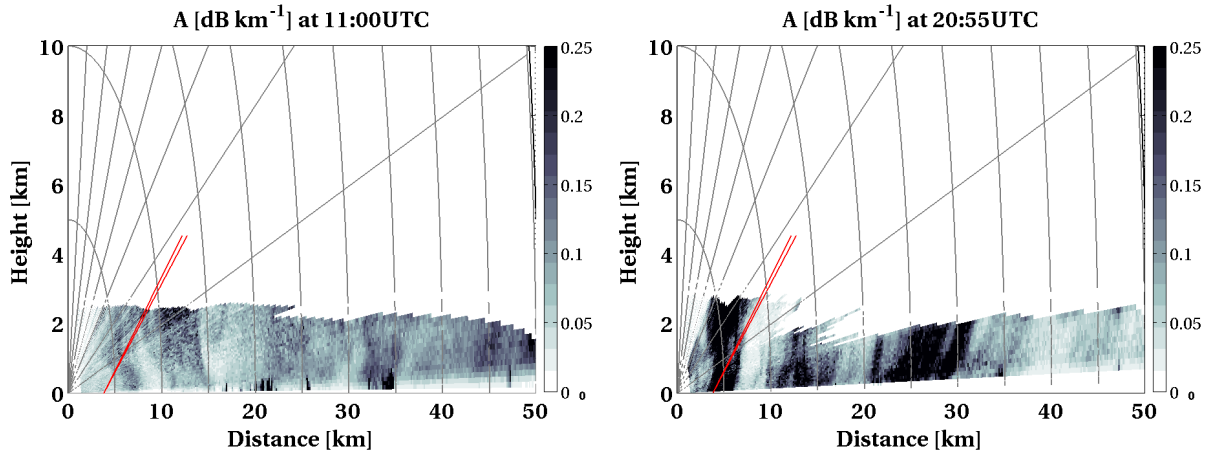


Figure 5: Results for the specific attenuation  $\text{dB km}^{-1}$  for RHI observations at 11:00 and 20:55 UTC, the red cone indicates the instantaneous radiometer's FOV.

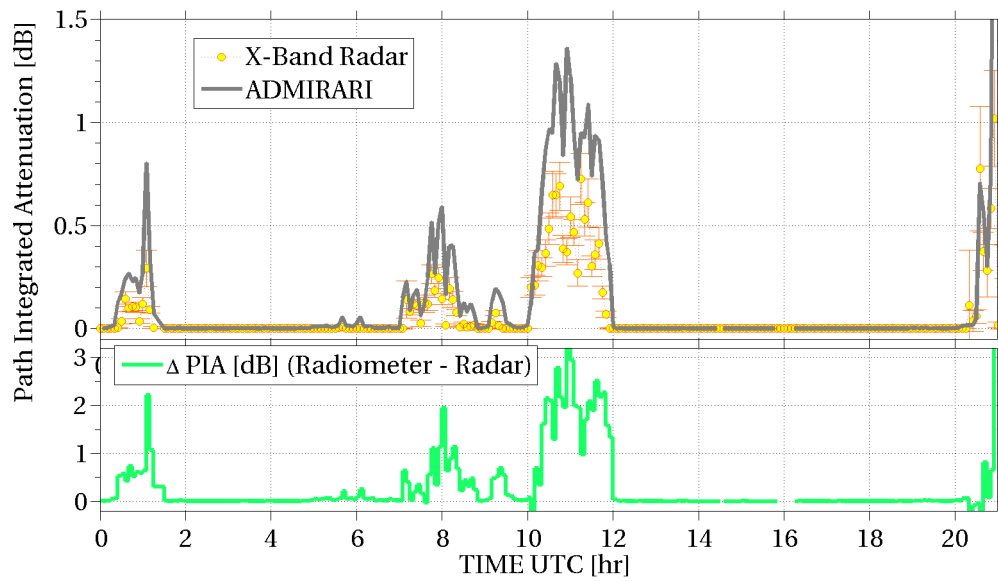


Figure 6: Time series for the retrievals of PIA at X-band from radiometer (gray solid line) and radar (yellow dots). The bottom panel indicates the difference between radiometer-radar PIA.

From figure 6 (bottom panel) a clear excess of radiometer's PIA during rain spans is obvious, with PIA residuals reaching as high as +3 dB for instance at 11:50 UTC, however the amplitude of that excess is rather not constant along the evolution of the rain event. The point to point comparison highlights better the difference between radiometer to radar retrievals (figure 7), with a systematic overestimation by the radiometer. Although a good correlation is found ( $r=0.92$ ) with a statistical bias (0.274 dB) and RMSE of 0.226 dB, a clear trend of PIA overestimation by the radiometer with a factor of  $m = 1.468$  (best-fit's slope red-dashed-line in figure 7) is also found.

The excess on PIA obtained by the microwave radiometer retrievals can be attributed to the radiative contribution from the atmospheric components above the rain layer, being the melting layer the most important at X-band. Since the radiometric contribution of the ice layer at X-band can be considered negligible, the residuals ( $\Delta \text{PIA}$ ) obtained in equation 5.1 are assumed due to the melting layer.

## 5.2. Extension to higher frequencies

By means of radiative transfer simulations for the optical thickness at the three ADMIRARI frequencies (10.7, 21.0 and 36.5 GHz), it is possible to find analytical relationships to map the attenuation from X-band to 21.0 and 36.5 GHz, according to the power law relationship

$$\tau_{\text{rain}}(\nu) = k_1(\nu)[\tau_{\text{rain}}(\text{X-band})]^{k_2(\nu)} \quad (5.2)$$

where  $\nu$  represents one of the higher frequencies.

Figure 8 depicts the ensemble of simulations utilized in the a-priori probability distribution function for the Bayesian estimation (section 3.2). The frequency pairs 10.7 versus 21.0 GHz are shown in the left panel and the pair 10.7 versus 36.5 GHz

in the right panel of figure 8. By fitting those points to the relationship in equation 5.2 the coefficients  $k_1(\nu)$  and  $k_2(\nu)$  are found, those are however dependent on drop size distribution (DSD) as it is shown by the coloured lines in figure 8.

Once the coefficients  $k_1(\nu)$  and  $k_2(\nu)$  are determined, the path integrated attenuation at 21.0 and 36.5 GHz can be estimated from the X-band radar retrievals. In table 3 a set of fitting coefficients are summarized for three DSD intercept parameters  $N_0$ , and for vertical and horizontal polarization.

The results of applying equation 5.2 with coefficients in table 3 for horizontal polarization are shown in figure 9 for the 21.0 GHz (left panel) and for 36.5 GHz (right panel). The figure shows the expected attenuation for 21.0 and 36.5 GHz considering a Marshall-Palmer distribution with  $N_0 = 8.0 \times 10^4 \text{ m}^{-3} \text{ mm}^{-1}$ .

In figure 9 the ADMIRARI retrievals at 21.0 and 36.5 GHz against the PIA obtained from equation 5.2 shows a slightly reduction on the best-fit slope with the increase of frequency from 1.47 to 1.36 and 1.28 for 10.7, 21.0 and 36.5 GHz respectively, indicating the distribution of point get closer to the one-to-one relationship, in other words the residuals for the higher frequencies tend to level-off to a constant value independent of the intensity of attenuation. On the other hand, the RMSE have larger values for higher frequencies with 1.06 and 2.64 dB for 21.0 and 36.5 GHz respectively, indicating that the estimation of rain layer attenuation at higher frequencies are prone to produce larger uncertainties since the results are compromised by resonant effects due to Mie scattering.

Every estimation of melting layer attenuation has also been flagged by the amount of rain water (LWP) and the thickness of melting layer (ML). The latest is estimated from the radar RHI scans using polarimetry techniques to determine the boundaries of the bright-band, while the rain LWP is obtained by using the ZPHI method according to Saavedra et al. (2013). In figure 10 is shown the scattering plots for  $\Delta\text{PIA}$  at 21.0 and 36.5 GHz versus the 10.7 GHz. Every retrieved value is represented by a box with different size and color, with the size of the box representing the amount of water in the rain layer (LWP) while the color corresponds to the thickness of the bright-band noting that color gray indicates no bright-band detected.

In figure 10 a general pattern is found, the boxes with detected bright-band are clustered around a line with different slope than those boxes with no bright-band detected. This is specially clear for cases with large rain LWP and no ML thickness detected (big-gray boxes), those point are notably separated by a different slope.

## 6. Conclusions

Synergistic observations at X-band by the passive microwave radiometer ADMIRARI and polarized weather radar have been used in order to estimate the melting layer's attenuation. In order to do so, a radiometer's field-of-view has been reproduced

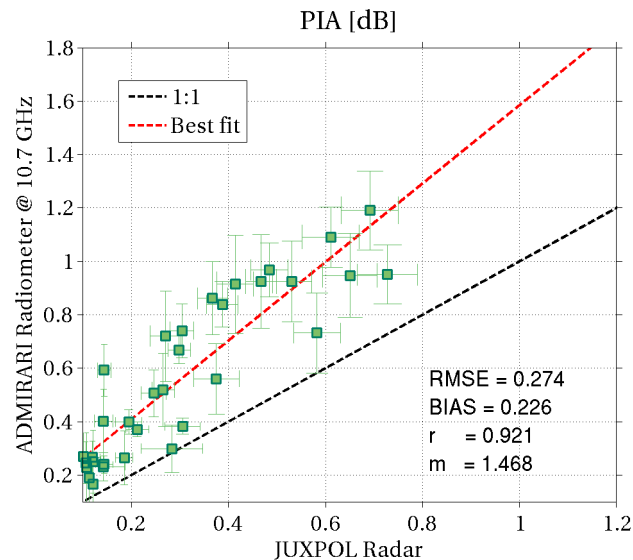


Figure 7: Point to point comparison of path integrated attenuation derived from synergistic observations by ADMIRARI and Dual-pol radar at X-band. Dashed-red line is the best fit, and the black-dotted represents the 1:1 comparison.

Table 3: Coefficients for power function 5.2, frequency dependent and for three DSD intercept parameter  $N_0$ .

DSD $N_0$ [ $\text{m}^{-3} \text{ mm}^{-1}$ ]		$32 \times 10^4$		$8 \times 10^4$		$4 \times 10^4$	
		$k_1(\nu)$	$k_2(\nu)$	$k_1(\nu)$	$k_2(\nu)$	$k_1(\nu)$	$k_2(\nu)$
21.0 [GHz]	H-pol	4.84	0.95	4.04	0.91	3.78	0.91
	V-pol	4.82	0.95	3.95	0.91	3.67	0.90
36.5 [GHz]	H-pol	14.43	0.88	10.07	0.82	8.74	0.80
	V-pol	14.38	0.89	10.06	0.82	8.76	0.80



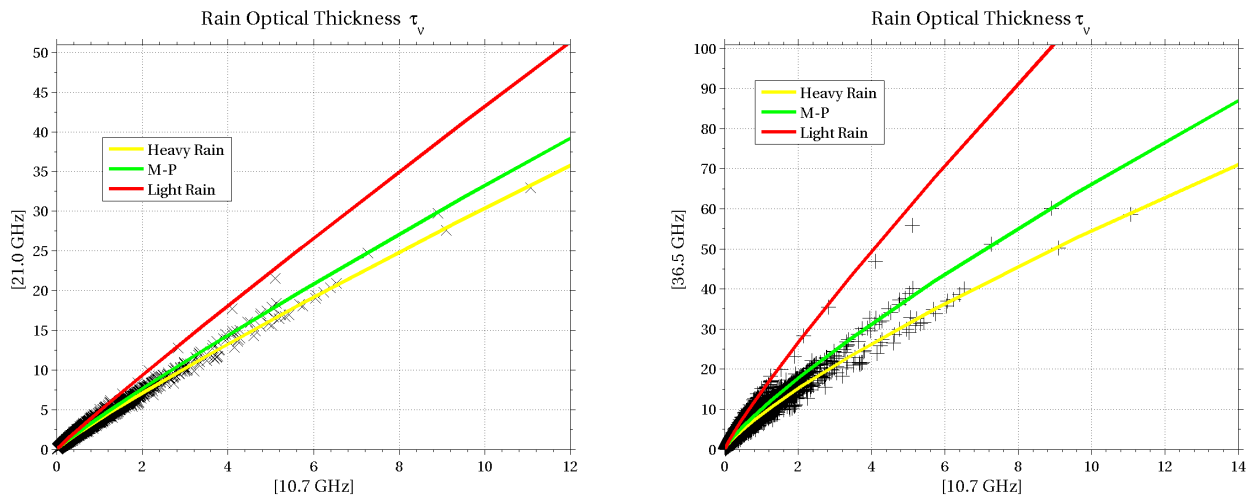


Figure 8: Power functions to map PIA from X-band to 21.0 GHz (left frame) and 36.5 GHz (right frame), the different color line represent a DSD with red for light-rain, yellow for heavy-rain and green for Marshall-Palmer.

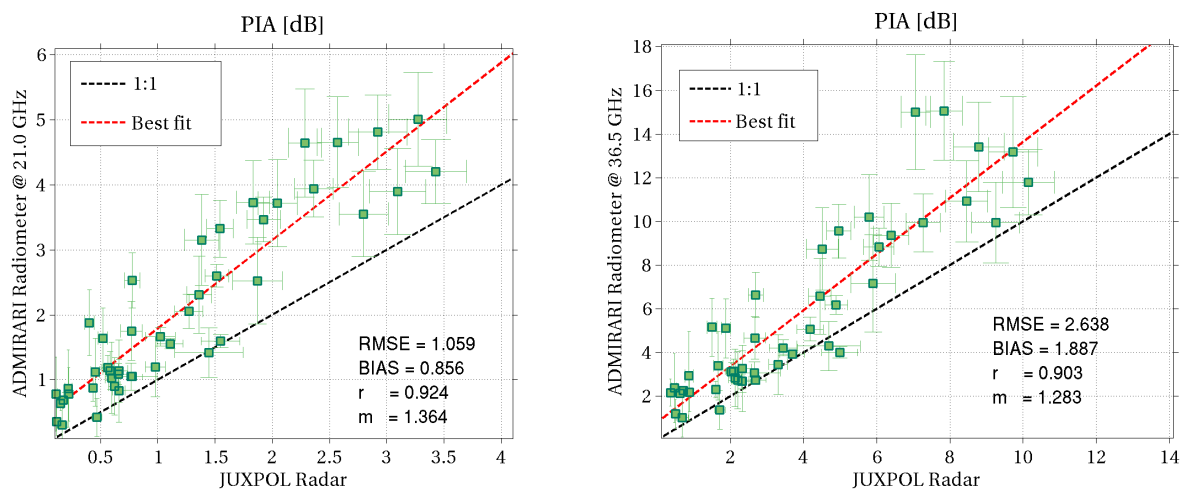


Figure 9: Same as figure 7, but for 21.0 GHz (left frame) and for 36.5 GHz (right frame) after applying the power function in equation 5.2.

out of radar RHI scans by considering realistic antenna beam-width and beam-pattern. Thereafter the standard radar variables are made available as they would have been observed by the radiometer.

The path integrated attenuation (PIA) was estimated by two different methods, i.e. Bayesian inversion for the radiometer and ZPHI algorithm for the radar. Both methods have been found to be feasible to estimate PIA when cases with strong polarization signal are considered. On the contrary neither method may produce accurate results when small raindrops do not have a well defined oblate shape to produce enough polarization difference that can be distinguished from the instruments noise level. Moreover, when the amount of water content is large enough to start saturating the radiometer's receivers, the information content is diminished with the consequence that the retrievals will largely differ from the radar's.

The novel approach used in this work paves the way to improve studies relating the multi-frequency signature for melting layer attenuation. The ambiguity introduced by DSD can be minimized by implementing a consistent estimation of rain drop-size parameters based on polarimetry methods, in which case a forward operator would need to be applied for every individual observation. Within the scope of the present work, the results have been put into consideration as a function of the three DSD intercept parameters.

## Acknowledgement

The ADMIRARI project is funded by the *Deutsche Forschungsgemeinschaft* (DFG) under grant SI 606/17-1. Special thanks to Dr. Birger Bohn from Jülich Research Center and Mr. Martin Lennefer from Meteorological Institute for their assistance with the instrumentation during the field experiment.

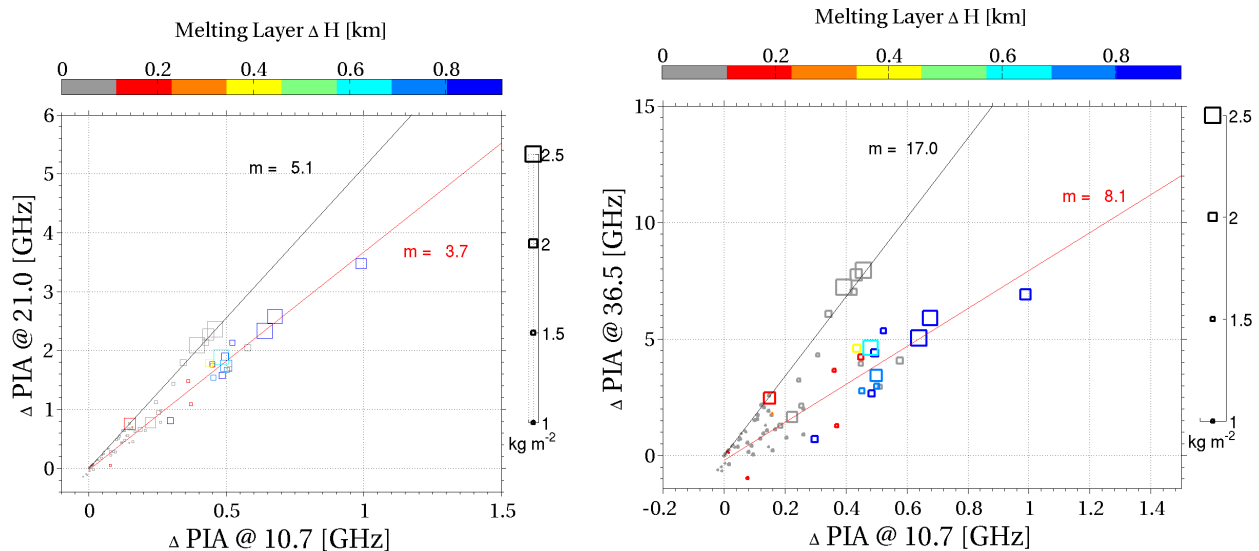


Figure 10: Difference of PIA from 21.0 GHz and 36.5 GHz versus 10.7 GHz. The boxes' size represent the amount of rain LWP and the color the slant thickness of the bright-band. The gray color indicates no bright-band detected.

## References

- A. Battaglia, P. Saavedra, C. Simmer, and T. Rose, "Rain observation by a multifrequency dual-polarized radiometer," vol. 6, no. 2, pp. 354–358, 2009, doi:10.1109/LGRS.2009.2013484.
- A. Battaglia, P. Saavedra, T. Rose, and C. Simmer, "Characterization of precipitating clouds by ground-based measurements with the triple-frequency polarized microwave radiometer ADMIRARI," vol. 43, no. 3, pp. 394–414, 2010.
- V. Bringi and V. Chandrasekar, Eds., *Polarimetric Doppler Weather Radar, Principles and applications*. Cambridge University Press, 2001, ISBN 0-521-01955-9.
- N. Gaussiat, R. Hogan, and A. Illingworth, "Accurate liquid water path retrieval from low-cost microwave radiometers using additional information from lidar and operational forecast models," vol. 24, pp. 1562–1575, 2007.
- F. S. Marzano, A. Mugnai, G. Panegrossi, N. Pierdicca, E. Smith, and J. Turk, "Bayesian estimation of precipitating cloud parameters from combined measurements of spaceborne microwave radiometer and radar," vol. 37, pp. 596–613, 1999.
- S. Matrosov, "Assesment of radar signal attenuation caused by the melting hydrometeor layer," vol. 46, no. 4, pp. 1039–1047, April 2008.
- C. Mätzler and J. Morland, "Refined physical retrieval of integrated water vapor and cloud liquid for microwave radiometer data," vol. 47, no. 6, pp. 1585–1594, 2009.
- S. McFarlane, F. Evans, and A. Ackerman, "A bayesian algorithm for the retrieval of liquid water cloud properties from microwave radiometer and millimeter radar data," *J. Geophys. Res.*, vol. 107(D15), p. 4271, 2002.
- A. Ryzhkov, M. Diederich, P. Zhang, and C. Simmer, "Potential utilization of specific attenuation for rainfall estimation, mitigation of partial beam blockage, and radar networking," vol. 31, no. 3, pp. 599–619, March 2014, doi: <http://dx.doi.org/10.1175/JTECH-D-13-00038.1>.
- P. Saavedra, A. Battaglia, and C. Simmer, "The contribution of the microwave radiometer ADMIRARI to the NASA GPM ground validation field experimetns," in *Proceedings of the International Radiation Symposium*. American Institute of Physics (AIP), August 2012, pp. 592–595. [Online]. Available: [http://proceedings.aip.org/resource/2/apcpcs/1531/1/592\\_1](http://proceedings.aip.org/resource/2/apcpcs/1531/1/592_1)
- , "Partitioning of cloud water and rain water content by ground-based observations with the radiometer ADMIRARI in synergy with a micro rain radar," *J. Geophys. Res.*, vol. D05203, no. 177, 2012, doi:10.1029/2011JD016382.
- P. Saavedra, A. Battaglia, A. Ryzhkov, and C. Simmer, "Synergy between polarimetric radar and radiometer ADMIRARI for estimation of precipitating parameters." American Meteorological Society (AMS), 2013. [Online]. Available: <https://ams.confex.com/ams/36Radar/webprogram/Paper229168.html>
- J. Testud, E. Le Bouar, E. Obligis, and M. Ali-Mehenni, "The rain profiling algorithm applied to polarimetric weather radar," vol. 17, pp. 332–356, 2000.